Materials Today Communications 27 (2021) 102428

Contents lists available at ScienceDirect

Materials Today Communications

journal homepage: www.elsevier.com/locate/mtcomm

The effect of milling time on the microstructure and mechanical properties of Ti-6Al-4Fe alloys

Hammadi Fouzia [a,b,c,*], Fellah Mamoun [b,d,*], Hezil Naouel [c], Aissani Linda [c], Mimanne Goussem [e], Mechachti Said [a], Abdul Samad Mohammed [f], Montagne Alex [g], Alain Iost [g], Sabine Weiß [h], Aleksei Obrosov [h]

[a] Metallurgy Department, Badji Mokhtar University, Annaba, B. O, 12 CP 23000. Algeria
[b] Tribology and Materials Group, Laboratory of Foundry, Badji Mokhtar University, Annaba, B. O, 12 CP 23000, Algeria
[c] Mater Sciences Department, ABBES Laghrour – University, Khenchela P.O 1252, 40004, Algeria
[d] Mechanical Engineering Department, ABBES Laghrour-University, Khenchela, P.O 1252, 40004, Algeria
[e] Laboratory of Materials & Catalysis, Djillali Liabes University, BP 89 Sidi-Bel-Abbès, 22000, Algeria
[f] Mechanical Engineering Department, King Fahd University of Petroleum and Minerals. Box 1180, Dhahran, 31261, Saudi Arabia
[g] Laboratory of Mechanics Surfaces and Materials Processing, ARTS ET METIERS ParisTech, 8, Boulevard Louis XIV, 59046, Lille Cedex, France
[h] Department of Physical Metallurgy and Materials Technology, Brandenburg Technical University, 03046, Cottbus, Germany

ARTICLE INFO

Keywords:
Ti-based alloys
Microstructure
Mechanical properties
Ball-milling
Biomaterials
Milling time

ABSTRACT

Replacement of toxic and expensive vanadium (V) in medical grade titanium alloys with cheaper and non-toxic elements such as iron (Fe) or niobium (Nb), is an important step forward in developing safer and less expensive biomaterials. Evaluating the effect of different process parameters such as the milling time on the properties of these newly developed alloys helps in understanding and controlling their behavior. Hence, in this study, the influence of ball-milling duration (2, 6, 8, 12 and 18 h) on crystalline structure, phase evolution, densification, and mechanical characteristics of biomedical nanocrystalline Ti-6Al-4Fe (wt. %) alloys is investigated. X-ray diffraction (XRD) confirmed that after 6 h of milling, aluminum (Al) and Fe completely dissolved into Ti matrix to form a solid solution of Ti (Al, Fe). XRD further revealed that the crystallite size decreased from 56 to 30 nm and the micro-strain increased with an increase in milling time. A decrease in porosity along with an increase in density is also observed for the alloys with increasing milling time. Moreover, the values of porosity obtained for the developed Ti-6Al-4Fe alloys ranged from 1 to 12 %, which is comparable to the porosity of one of the cortical bones making it a potential candidate for bone replacements. Microhardness measurements showed that the hardness of the Ti-6Al-4Fe alloys was greater than the hardness of the conventional Ti-6Al-4V alloys. It was observed that the Ti-6Al-4Fe alloy fabricated with the powders milled for 2 h showed the lowest value of Young's Modulus. Milling time also had a significant effect on the surface roughness of the alloy samples, which showed a decreasing trend with increasing milling times.

1. Introduction

Medical grade titanium alloys are being used extensively in biomedical applications due to their outstanding biocompatibility [1,2], high corrosion resistance [3–5], minimal cellular reaction [3,6] and good osseointegration [4]. However, they do suffer from a few limitations such as poor mechanical strength [5–8].

Among the many available Ti alloys, Ti-6Al-4V alloys in particular have found their way in traumatic and orthopedic applications due to their good property combination and better corrosion resistance as compared to Co-Cr-Mo alloys and stainless steels. Even though they have excellent strength and toughness, there is still a huge discrepancy between the mechanical behavior of Ti-6Al-4V alloy and cancellous / cortical bone, which results in stress-shielding effect and loosening of a bone end graft.

Furthermore, the presence of a toxic element like vanadium (V) [9–11] leaching into the body, which raises long-term biocompatibility concerns, coupled with its high cost and less formability, limits the

* Corresponding authors at: Tribology and Materials Group, Laboratory of Foundry, Badji Mokhtar University, Annaba, B. O, 12 CP 23000, Algeria.
E-mail addresses: Hammadi.fou@yahoo.fr (H. Fouzia), mamoun.fellah@yahoo.fr (F. Mamoun).

https://doi.org/10.1016/j.mtcomm.2021.102428
Received 27 April 2020; Received in revised form 21 April 2021; Accepted 5 May 2021
Available online 9 May 2021

practical utilization of Ti-6Al-4V alloys. One of the routes by which the above mentioned drawbacks can be overcome is, by replacing V with cheaper, less toxic and workable additives such as iron (Fe) and niobium (Nb) [12,13]. These two alloying elements are the most effective β phase stabilizing elements for Ti alloys [14,15], which help to improve their crack resistance and mechanical properties.

Recently, Iron has gained a lot of attention as a dopant in various alloys for biomedical applications [16–20]. In one of our previous works, V was replaced by Fe and Nb in (α + β) Ti-6Al-4V alloys and the effect of these replacements on their structural and mechanical properties was evaluated [16]. In another study, a significant improvement in the mechanical properties was observed for an iron content between 1–4 wt. % [12,17]. The Young's modulus decreased in the Ti-6Al-xFe alloys with increasing iron content, while the Ti-6Al-2Fe and Ti-6Al-4Fe alloys showed superior mechanical properties [18]. Effect of iron addition in Ti-12Mo-6Zr-xFe alloys revealed an increased β phase stability with improved mechanical properties [19]. Hence, Ti-6Al-4Fe alloy, which exhibits similar properties to those of Ti-6Al-4V alloy in terms of its chemical stability, corrosion resistance, mechanical properties, and easy control of its microstructure [21], has a great potential to be used as a biomaterial.

Various methods such as solidification/casting, forging, sintering, and powder metallurgy are used for fabricating Ti based alloys [10]. However, powder metallurgy, helps to produce materials having weak-to-absent texture, fine grain (nanocrystalline) structure with high homogeneity in comparison to the conventional wrought one [20].

To develop nanocrystalline alloys by powder metallurgy, nanostructured powders are to be synthesized. Mechanical alloying (MA) is one of the available techniques to synthesize these nanostructured powders by a process of repetitive fracturing, welding and re-welding of powder particles [22–24]. A planetary ball mill is commonly used for mechanical alloying, to produce ultra-fine and homogeneous powders [24–26]. Various milling parameters such as milling time, ball-to-powder ratio (BPR), rotational speed, process controlling agent (PCA), milling environment etc. could be applied to affect the process and resulting properties [24,26,27].

One of the most significant parameters to achieve an equilibrium between the cold-welded and fractured powder particles is the milling time, which results in relatively coarse and stable particles [28]. The impact of ball milling time on the structural properties of Ti-6Al-7Nb alloys was extensively studied and reported in our previous work and was found to be the most significant parameter in the development of these alloys [4]. However, no such study has been reported for the Ti-6Al-4Fe alloys.

Hence, the current study focuses on the development of Ti-6Al-4Fe alloys for biomedical applications, such as dental implants and hard tissue replacements and evaluation of the effect of ball-milling time on the morphological and phase changes, occurring during the milling of Ti-6Al-4Fe powders. Furthermore, the effect of milling time on total porosity and density of the compacted and sintered powders is also investigated.

2. Materials and experimental methods

2.1. Sample preparation

Nanostructured Ti alloy powder was prepared by mixing / grinding, Ti, 6 wt.% of Al and 4 wt.% of Fe powders together in a high-energy ball mill, Fritsch P7 (Planetary Micro Mill Pulverisette 7, Fritsch GMBH, Germany) The elementary powders of titanium (Ti) (99.99 % pure), aluminum (Al) (99.98 % pure), and iron (Fe) (99.97 % pure) were procured from Alfa - Aesar Society, Germany. Their characteristics and compositions are presented in Table 1.

The powders were weighed and ball milled for 2, 6, 12 and 18 h respectively, in hardened agate cylindrical vials of 80 mL capacity using a milling speed of 450 rpm. Agate balls of 10 mm diameter with a ball to powder ratio of 10:1 were used during the ball milling process. The milling was carried out in cycles of 20 min with a pause of 10 min in between the cycles in air (i.e. the vials were not filled with an inert gas during the milling process). The vials were opened after a 35- to 40-min cooling period, after each milling operation. To avoid sudden contact of the milled powders with oxygen, which may lead to ignition or oxidation, the opening and closing of the vials is done in a chamber under a controlled atmosphere of argon.

Table 1
Characteristics of the as-received powders and their chemical composition in Ti-6Al-4Fe.

Property	Titanium	Iron	Aluminum
Melting temperature (K)	1943	1809	933
Particle size (μm)	100 ± 10	45 ± 4	10 ± 1
Particle morphology	Spherical	Irregular	Spherical
Chemical Composition (wt. %)	Balance	4	6

The milled powders were uniaxially pressed using an Elvc Hydraulic press at room temperature at a constant strain rate under a pressure of 100 MPa to obtain cylindrical samples of 15 mm diameter using a rigid steel die. This green body was subsequently hot pressed at 150 MPa and at a temperature of 1050 °C in an argon atmosphere for 30 min to obtain a closed porosity using an ASEA-HIP (QIH-6) machine. The hot isostatically pressed (HIPed) samples were then subjected to sintering, at a temperature of 1150 °C for 1 h to remove any stress concentrations [16].

2.2. Sample characterization

2.2.1. Structural characterization

The powder morphology was characterized using a scanning electron microscope (Philips XL 30 ESEM FEG), with the following imagining details: Accelerating high voltage (HV) = 25 KV, horizontal field width (HFW) =497 μm, and Working distance (WD) = 14.2 mm. EDS-analysis voltage: 15 kV and measurement duration of 600 s per point. The average grain size of the milled powders was also measured and analyzed using SEM [1, 40 and 41]. The size of all ball-milled alloy powders was measured using a particle size analyzer (Microtrac S3500 laser diffraction, Microtrac Inc., USA).

Energy-dispersive spectroscopy (EDS) with Si (Li) Detector and ZAF corrections of intensity ratios was used to determine the chemical elements to estimate their relative concentrations (quantitative analysis). The relative concentrations were estimated by Eq. 1 [29]:

$$\frac{C_{spec}}{C_{std}} = ZAFc.\left(\frac{I_{sp}}{I_{st}}\right) = ZAFc.K\text{-}ratio \quad (1)$$

Where Z is the "atomic number correction," A is the "absorption correction," and F and c are the "secondary fluorescence corrections" for characteristic (F) and bremsstrahlung or continuum (c) radiation, respectively.

$\frac{C_{spec}}{C_{std}}$ is the relative concentration of the element in specimen and in standard and

I_{sp}/I_{st} corresponds to the relative intensity of spectral lines (equal to *K-ratio*);

The absorption bands were analyzed by Fourier transform infrared spectroscopy (FTIR) using a Platinum ATR, from 400 to 4000 cm^{-1} with an increment of 4 cm^{-1}.

The lattice parameter and phase identification was performed using XRD measurements (Rigaku D-MAX) at 40.0 KV and 35 mA with Cu-K_α radiation. A scan range of 20 – 90° with an increment of 0.02° and a scan time of 1 s/step were used. The crystallite size was determined by the broadening of the diffraction peaks with ±5 nm accuracy using Scherrer's formula [30]:

$$D = \frac{0.9\,\lambda}{\beta cos\theta}; \quad (2)$$

While, the lattice-strain was determined by the classical Williamson–Hall (W–H) equation [31]:

$$\beta cos\ \theta = \frac{0,9\ \lambda}{D} + 4\varepsilon sin\ \theta \quad (3)$$

Where 0.9 is the shape factor, λ represents the X-ray wavelength ($\lambda_{Co} = 0.178$ nm), β is the line width (FWHM) in radians, θ is the Bragg's angle, ε is the micro-strain and D is the crystallite size.

2.3. Mechanical characterizations

2.3.1. Density and porosity measurement

The density of the compacted and sintered samples was measured by the Archimedes principle. The actual density of the sample was:

$$\rho = [a/(a\text{-}w)] \quad (4)$$

Where a and w are the masses of the samples in air and in water, respectively and ρ is the density of water. The theoretical density of the compacted and sintered samples was calculated by the mixture rule, based on the starting compositions of the samples.

The characteristic pore parameters were determined by quantitative analysis of micrographs using Image-Pro Plus software (Annaba, Algeria) and was also confirmed using the equation below [32].

$$P = \left(1 - \frac{\rho_{sint}}{\rho_{th}}\right) \times 100\ \% \quad (5)$$

where ρ_{th} is the density of compact Ti-6Al-4Fe (4.532 g/cm^3) and ρ_{sint} is the density of the sintered samples.

2.3.2. Young's modulus and microhardness measurements

Young's modulus and microhardness of compacted and sintered samples were measured using a Vickers microindenter (ZWICK $ZHV_{0.2}$, G, Lille, France) by applying a 50 g load for a dwell time of 10 s on the sintered samples, polished with 2 μm diamond paste. Six measurements were taken for each sample while maintaining the distance between two indents to be at least 3 times the indent size to avoid interaction between the hardness indents. The Young's modulus measurements were determined from the linear part of the compression stress-strain plot [33].

2.3.3. Roughness analysis

The roughness of the compacted and sintered samples was measured using a Veeco Wyko profiling system (NT1100 – Lille, France) with 5 mm tip radius with a maximum traversing length of 25 mm and maximum vertical range of 500 mm. The resolution was 1 nm for horizontal measurements and 10 nm for vertical ones. The average surface roughness (R_a) was calculated in accordance to ISO 4287 standard [34].

3. Results and discussion

3.1. Physical characterization

3.1.1. Morphological analysis of the powders

SEM micrographs of the as-received powders as shown in Fig. 1, demonstrate that both, Ti and Al powder particles are spherical, and the iron particles are irregularly shaped.

The particle morphology of the milled powders with different ball-milling times is presented in Fig. 2. It is well known that the ball-milling process comprises of three main phases: (i) cold welding, (ii) fracturing and (iii) stability [35].

As can be clearly seen from Fig. 2, the particle size distribution becomes more homogeneous with increasing milling time. After 2 h of milling, irregularly shaped particles with a broad particle size distribution between 14 μm–60 μm is observed as shown in Fig. 2(a). This can be attributed to insufficient milling time for particle size homogenization.

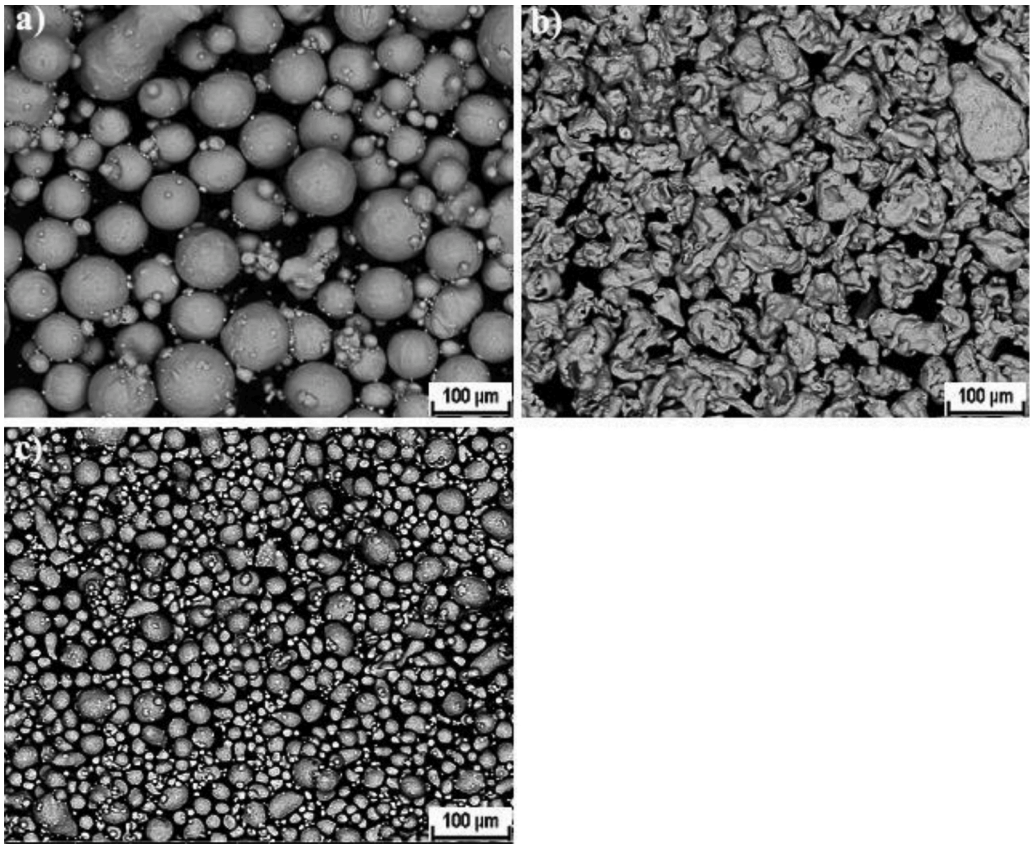

Fig. 1. SEM micrographs of the as received powders of pure (a) titanium (Ti), (b) Iron (Fe) and (c) Aluminum (Al).

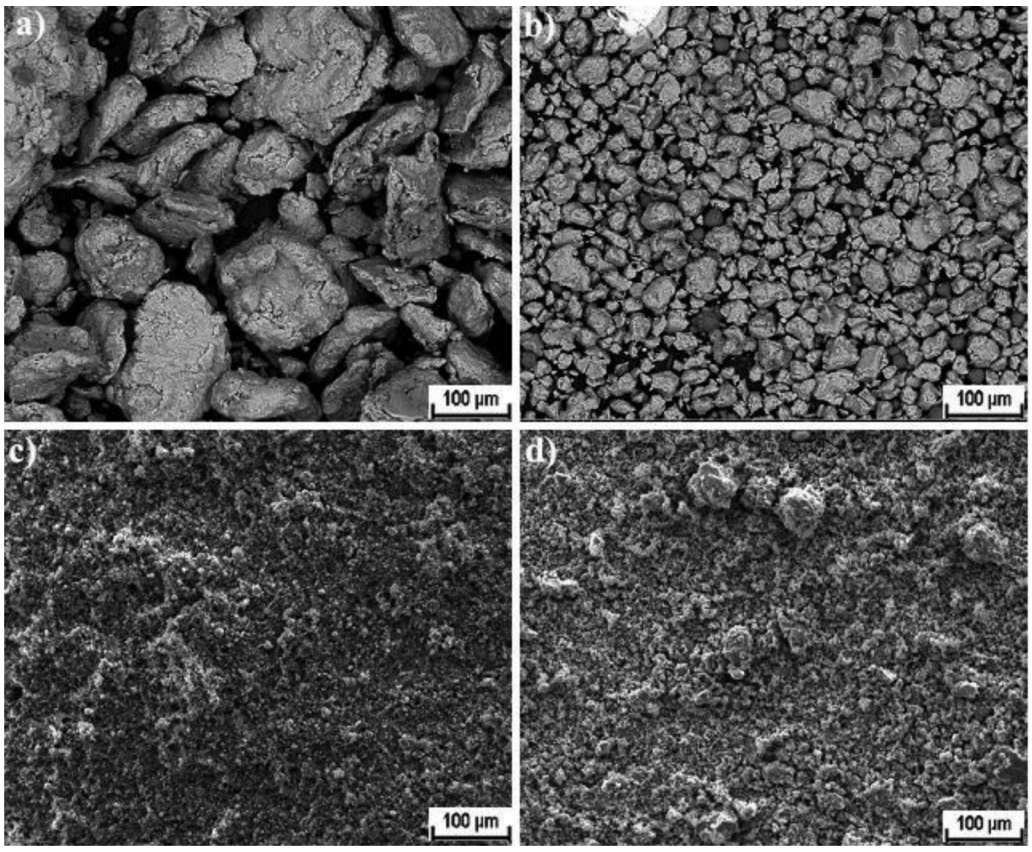

Fig. 2. SEM. Morphology of the powders after a) 2 h, b) 6 h, c) 12 h and d) 18 h of ball-milling.

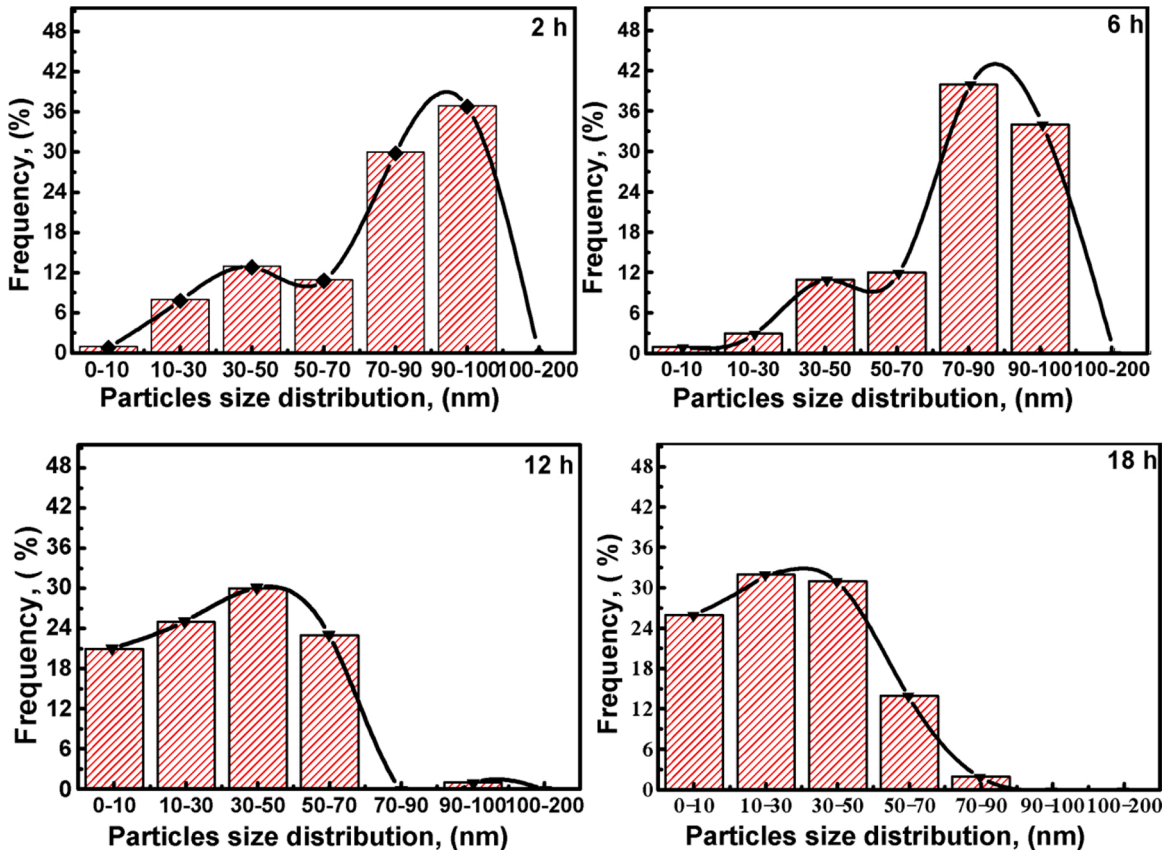

Fig. 3. Particle-size distribution graphs of milled titanium alloy Ti-6Al-4Fe as a function of milling time measured by laser diffraction/scattering method.

After 6 h of milling, irregularly flake-shaped particles were observed (Fig. 2(b)). However, only small quantities of Al and Fe were embedded into the Ti powder [30]. They were bonded mechanically as reported in [36], because the increased milling time results in increased stress and accumulation of energy.

As the ball-milling time increased from 6 to 12 h, a large quantity of flake shaped particles split into smaller particles of equiaxial morphology, resulting in a significant reduction in average particle size (Fig. 2(c)). It has been reported that, an equiaxed morphology of the powder results in high strength and improved ductility with a reduction in fracture toughness of the finished samples, while a lamellar powder morphology helps in improving the fracture toughness with a reduction in ductility and strength [37].

After 18 h of milling (Fig. 2(d)), the finely split particles were agglomerated resulting in a reduced specific surface area. As reported previously, the reduction in particle size and increased homogeneity is a result of an equilibrium between cold-welding and fracturing during the milling process [16]. The particle sizes are reduced when the dominant mechanism is plastic deformation, whereas particle sizes increase when cold-welding is dominant [38].

The particle size distribution after different milling times is given in Fig. 3. For short milling times, (2 h and 6 h), a size distribution with two peaks: a small one at 30−50 nm (10 vol. % of the particles) and a large one around 90 nm (90 vol. % of the particles) occurs with slightly decreasing tendency for 6 h milling time. After 12 h of milling, the particle size significantly decreases and the particle size distribution is more uniform. 80 vol. % of the powder consists of particles smaller than 60 nm and 20 vol. % of the particles are even smaller than 5 nm. Few larger particles remain at high milling times, probably due to the agglomeration of particles. After 18 h of milling, the particles appeared to be flattened due to high milling energy induced micro-forging processes. The mean particle size was reduced to 30 nm due to the predominance of fracturing of the powder particles during the cold welding process. With respect to the initial powders, the particles were more uniform in size.

The elemental compositions of the Ti-6Al-4Fe alloys after different milling times analyzed using EDX (Table 2) were in good agreement with the nominal compositions. The percentage of O and N is difficult to quantify by this method, but an increasing tendency, due to O and N contamination from the ambient atmosphere during milling [39] is obvious.

It is often reported in the literature on mechanical alloying [10,11], that, milling leads to a significant increase in the O content. Severe sticking during prolonged milling requires scraping off the powders from the walls of the vials using milling tools at frequent intervals. Scraping, however, is a time consuming process and, if performed too aggressively, can lead to contamination of the powders by incorporation of particles from the milling tools.

It is clear from Table 2, that milling of the elemental powders led to a significant increase in O concentration, and possibly also to small increases in N. The O levels are similar to the levels reported by Kim et al. [17] after milling elemental powders of Ti and Al. This contamination, which is commonly attributed to the milling atmosphere [18], is difficult to prevent because of the high reactivity of elements such as Ti and Al. By comparison, the pre-alloyed powders, which are expected to be less reactive, had a much lower O and N content than the elemental powders, and these low impurity concentrations were maintained during milling.

Table 2
EDS analysis of milled Ti-6Al-4Fe powder particles, as a function of milling time.

Element	Ti (Wt.%)	Al (Wt.%)	Fe (Wt.%)	N (Wt.%)	O (Wt.%)
2 h	66.04	19.54	2.36	2.03	10.03
6 h	67.32	14.54	2.82	4.98	10.34
12 h	74.51	11.40	3.40	0.01	10.68
18 h	77.23	5.28	2.49	4.64	10.36

On the other hand, the N contamination may result from (1) N existing in the as-received titanium; or (2) adsorption and/or absorption of N during the exposure of the milled powder to air [12]. During mechanical milling, the remaining air in the powders would serve as a source of a reaction gas. As a result, this may have led to the formation of titanium nitride [19].

3.1.2. FTIR analysis

The FTIR peaks of the milled powders for different ball-milling times are presented in Fig. 4. In all spectra, bands assigned to the stretching vibrations of the O—H groups (≈ 3433–3675 cm^{-1}) together with bending vibrations in H_2O molecules (≈ 1631 cm^{-1}) are observed [40–42]. Furthermore, these profiles revealed the presence of carbonate.

The carbonate vibration bands of C—O (871 and 1420 cm^{-1}) could be related to the adsorbed carbon dioxide on the solid surface [43]. The presence of H_2O and CO_2 is possibly due to the sample's exposure to atmospheric air.

The peak at 2361 cm^{-1}, corresponds to the C—H stretching bands. Fig. 3 shows that the C–H stretch is very intense, indicating the existence of a large quantity of aliphatic hydrocarbons as these materials are composed of various organic contaminants, mainly aliphatic hydrocarbons. Song et al. [44] confirmed that the peaks appearing in the regions of (2850–2853 cm^{-1}) and (2923–2926 cm^{-1}) display the presence of organic carbon in all samples after milling.

Connected bands with Ti—O vibration bonds occur in the ranges of 420–620 cm^{-1} and 669–720 cm^{-1}. Sabataityté et al. [43] determined the absorption strip of the Ti—O—Ti bonds at 440 cm^{-1}. Ajmal et al. and Takafuji et al. [46,47] reported that M—O and M—O—M bond vibrations can be observed in the range of 800–450 cm^{-1}.

3.1.3. XRD analysis

To obtain further information about the crystal structure, XRD analysis was conducted. XRD peaks of the milled powders for 2–18 h are shown in Fig. 5. As confirmed previously by Suryanarayana et al. [23], formation of the Ti-6Al-4Fe alloy is completed after a few minutes (3–10) of milling [48]. Thus, the elemental peaks disappear with increasing milling time and peaks corresponding to solid solution phases slowly start to appear.

After 6 h of milling, Al and Fe peaks disappear, confirming that Al and Fe have dissolved into Ti to form a solid solution of Ti (Al, Fe) [30]. Meanwhile, with increasing milling time a broadening of the Ti peak and a reduction in its intensity was observed, which is attributed to a decrease in crystallite size from 56 μm to 30 μm and an increase in internal lattice strain. Another reason for the reduction in peak intensities may be the amorphous nature of the ball-milled material [49].

A peak shift of titanium towards lower angles was also observed which is attributed to an increase in the Ti lattice parameters, due to Al and Fe dissolution within the Ti lattice as confirmed by Han et al. [50]. The trend for the shift to lower angles of the Ti peak is most pronounced for the Ti (101) peak. This shift can be an indication of a considerable decrease in crystallite size and an increase in lattice strains. Sakher et al. [51] reported a broadening and shifting to lower angles of the peaks due to the intersection of XRD patterns from different phases, suggesting an increase in interatomic distances resulting in the expansion of the unit cell.

The crystallite size continuously decrease and reach the lowest value for powders, milled for 18 h. The X-ray pattern for the Ti-6Al-4Fe samples showed diffraction peaks corresponding to the (α + β) phases; body centered cubic (bcc) (β-phase) and compact hexagonal (hcp) (α-phase).

Similar results were obtained by X-ray diffraction in [22,52,19], indicating that Ti-6Al-xFe, Ti-5Al-2.5Fe and Ti-Mo-Zr-Fe alloys consist of α phase (hcp structure) as well as β phase (bcc structure).

3.1.4. Lattice parameter analysis

The lattice parameters, 'a' and 'c', of the Ti-6Al-4Fe alloys milled at

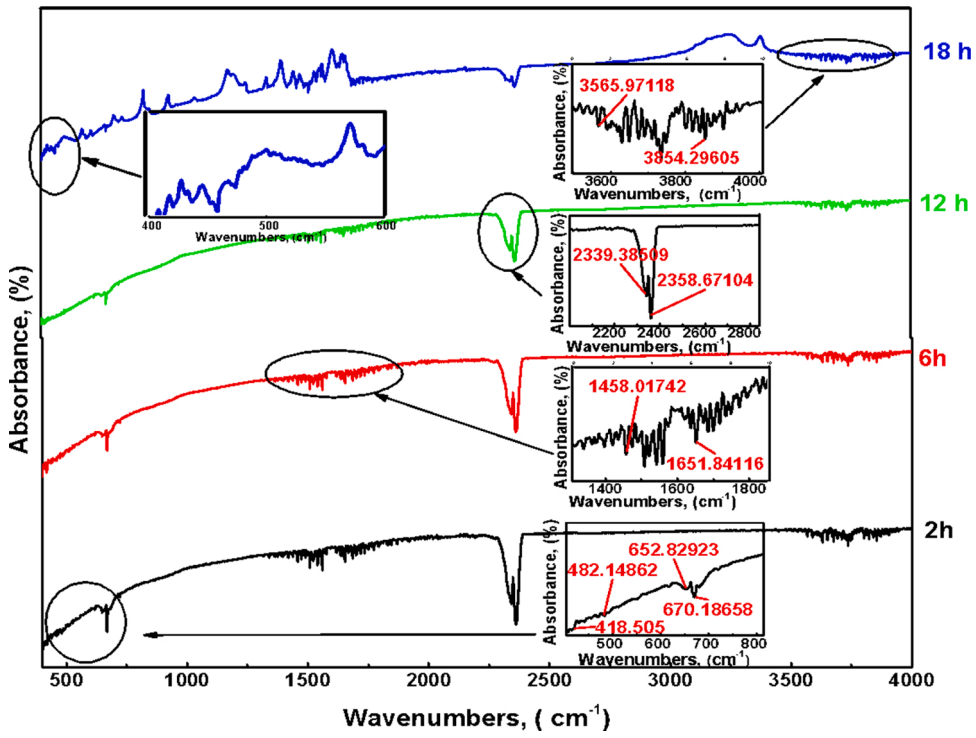

Fig. 4. FTIR spectra of Ti-6Al-4Fe milled powders for different milling times.

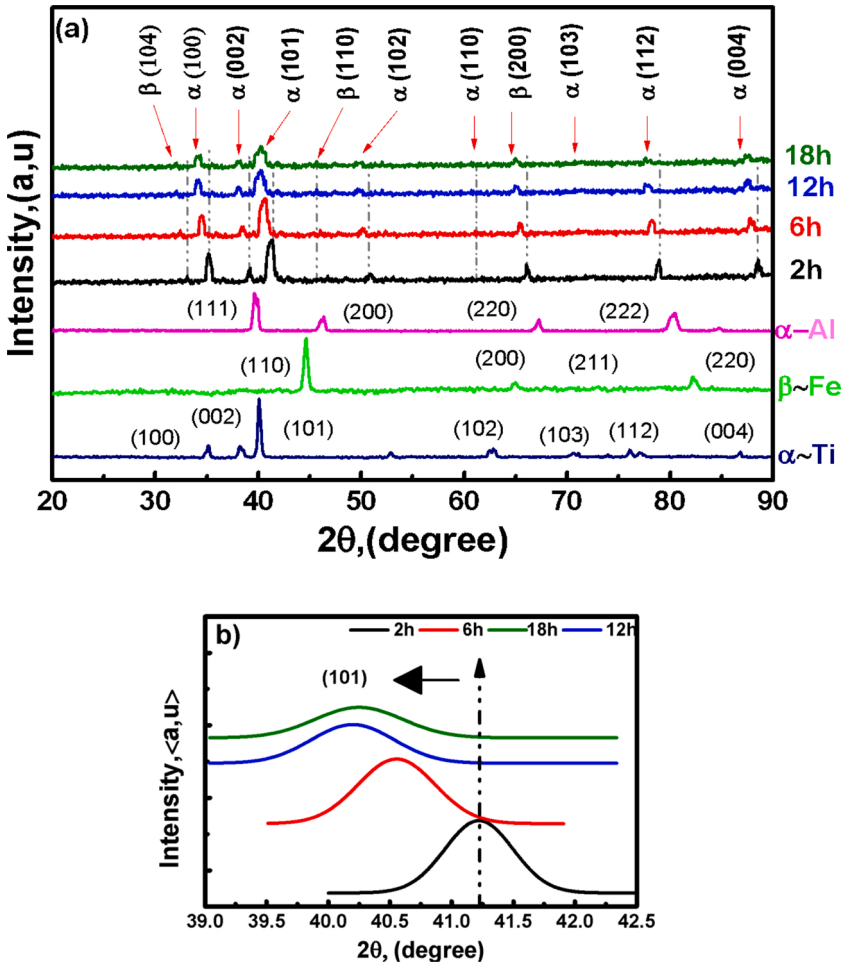

Fig. 5. (a) XRD patterns of the Ti-6Al-4Fe powders, milled for 2 h to 18 h. (b) Enlarged presentation of the shift.

2, 6, 12 and 18 h, respectively, are shown in Fig. 6. The lattice parameters grow with increasing milling time. This increase can be attributed to the difference in size between the solvent atoms of titanium and the solute atoms of aluminum. As the atomic radius of titanium ($r_{Ti} = 1.47$ Å) is larger than the one of aluminum ($r_{Al} = 1.43$ Å), aluminum dissolves in titanium and a substitution of aluminum and iron atoms by larger titanium atoms [22,23,53] takes place, which introduces higher distortions in the lattice, resulting in an increase in lattice parameters [22,23,54].

The crystal lattice distortion is calculated by $(\Delta a = \frac{a-a_o}{a_o})$, where a_0 and a are the lattice parameters before and after ball-milling. With an increase in ball-milling time from 2 h to 18 h, the lattice parameters (a_β, a_α & c_α) tend to grow due to: (i) formation of a compound by mechanical milling (solid-solution formation) (ii) the introduction of first-order internal stresses, and (iii) decreasing oxygen pressure [34,55].

All of the lattice parameters increased with increasing milling time. According to literature, two phases for the development of crystallite size, microstrain and lattice parameters for materials prepared by high-energy milling are reported. In the first milling phase the crystallite size decreases, whereas in the second phase a stable value is reached [5,7]. If the lattice parameters do not reach a stable value, it indicates that the alloying process was not completed even if XRD revealed Fe and Al peaks.

No crystals smaller than several nanometers embedded in a matrix were recognized, which suggests that the present milling times failed to create enough quantity of dislocations in the material in order to fully dissolve elements in the Ti lattice [56]. Cell volume expansion can be attributed to the introduction of various defects such as dislocations, stacking faults and vacancies produced by severe plastic deformation [16].

3.1.5. Crystallite size and microstrain analysis

As mentioned above the crystallite size was determined using Scherrer's equation. The lattice strain was determined by the classical Williamson–Hall (W–H) plots, by plotting $\beta \cos\theta$ as function of $4 \sin\theta$ for powders, ball-milled for different times. The lattice strain ε is the slope of the linear fitted line (Fig. 7).

The evolution of crystallite size and lattice strain of the ball-milled powders is displayed in Fig. 8. According to the observations, the crystallite size decreases from 56 nm to 30 nm with increasing ball-milling time from 2 h to 18 h, which is in good agreement with the literature [57,58].

Fig. 7 shows that the lattice strain significantly increased after 2 h of ball-milling. However, the strain rate slowed down between 6 h and 12 h of milling. Lattice strain increases significantly after 2 h of milling, which is attributed to the dislocation formation during longer milling time [59].

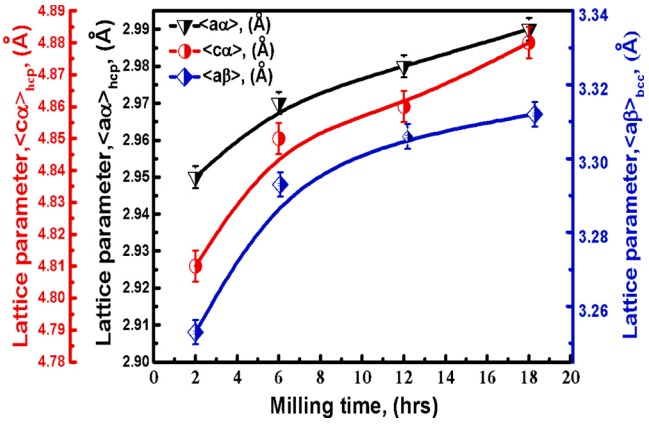

Fig. 6. Evolution of lattice parameters: < aα >, < aβ > and < cα >, (Å) of the Ti-6Al-4Fe milled powders versus milling time.

Some authors confirmed that lattice-strain increase can be related to a reduction in crystallite size, which is in agreement with the present study (Fig. 8) [58], too. The lattice-strain value rises with increasing milling time as reported in [60] and due to the increasing dislocation density, the average atomic strain increases as well. The grains split into smaller grains, separated by low angle sub-boundaries, as the dislocation density approaches a critical value.

Due to severe plastic deformation the misorientation between subgrains increases and low angle grain boundaries are replaced by high angle grain boundaries leading to the formation of nanocrystalline particles [61,36].

Dercz et al. [62] reported that during milling, broadening of the diffraction peaks of the milled powders and decrease in their intensities are associated with an increase in internal lattice strain and a decrease in crystallite size. According to Dong et al. [63], the formation of shear bands is the most significant deformation mechanism during the ball milling process. Similar to Avar et al. [61] in this work crystallite size decreases significantly in the early stage of the milling process and afterwards tends to stabilize at higher milling time.

3.2. Mechanical characterization

3.2.1. Density and porosity measurements

Fig. 9 illustrates the variation in experimental porosity and relative density of compacted and sintered Ti-6Al-4Fe samples for different milling times. Increasing milling time results in lower porosity of the sintered samples. The structures obtained in this study were having porosity in the range of 1–12 %, depending upon the milling time. Since the targeted biomedical application of the developed alloy is bone replacement, its structure has to be comparable to that of bones/tissues. According to the literature, the bone-tissue can have two different types of structures: one similar to the cortical bone, which is quite dense (5–10 % of porosity) and the other similar to the cancellous or trabecular bone, which is very porous (75–85 % of porosity) [64]. It can be observed that, the porosities obtained in this study are between 1 % and 12 %, which are comparable to that of the cortical bones, making it a potential candidate to be used for bone replacement.

Dercz et al. [65] showed that porosity values obtained by the Archimedes method are lower than the ones measured by image analysis due to incomplete participation of the enclosed pores [65]. The formation of pores, in particular, an interconnected system of pores, allows infiltration of cells and body fluids into the porous body, creating tissular variants by cell differentiation resulting in indirect osteogenesis. Certain pore sizes and predetermined pore size distributions are highly beneficial in sustaining steady cell proliferation and tissue growth at various in vivo stages, as reported in [66].

Siguira et al. [20] investigated Ti-5Al-2.5Fe (α + β) alloys by replacing vanadium with iron because of the detrimental effect of V on the biological systems. They reached a relative density (RD) of 96 % for this alloy, which was fabricated by powder metallurgy followed by sintering at 1400 °C. Simsek and Ozyurekr [69] measured a RD of 96.9 % for a Ti-5Al-2.5Fe alloy produced by mechanical alloying. Yamanoglu et al. [70] measured a RD of 98 % for the Ti-5Al-2.5Fe alloy fabricated by MA and hot pressing techniques. These results are comparable to the ones obtained in this study.

3.2.2. Influence of milling time on microhardness and Young's modulus

Fig. 10 shows the variations in hardness and Young's modulus of sintered samples as a function of milling time. The microhardness of the sintered Ti-6Al-4Fe samples shows an increasing trend with longer milling times.

Hardness values of the sintered samples made of powders milled for 2 h, 6 h, 12 h and 18 h were measured to be 335 ± 17 $HV_{0.05}$, 387 ± 19 $HV_{0.05}$, 475 ± 23 $HV_{0.05}$ and 660 ± 33 $HV_{0.05}$, respectively. These results are similar to the findings of Chen and Zhang [53]. The linear increase in microhardness of sintered samples with milling time of the powders is

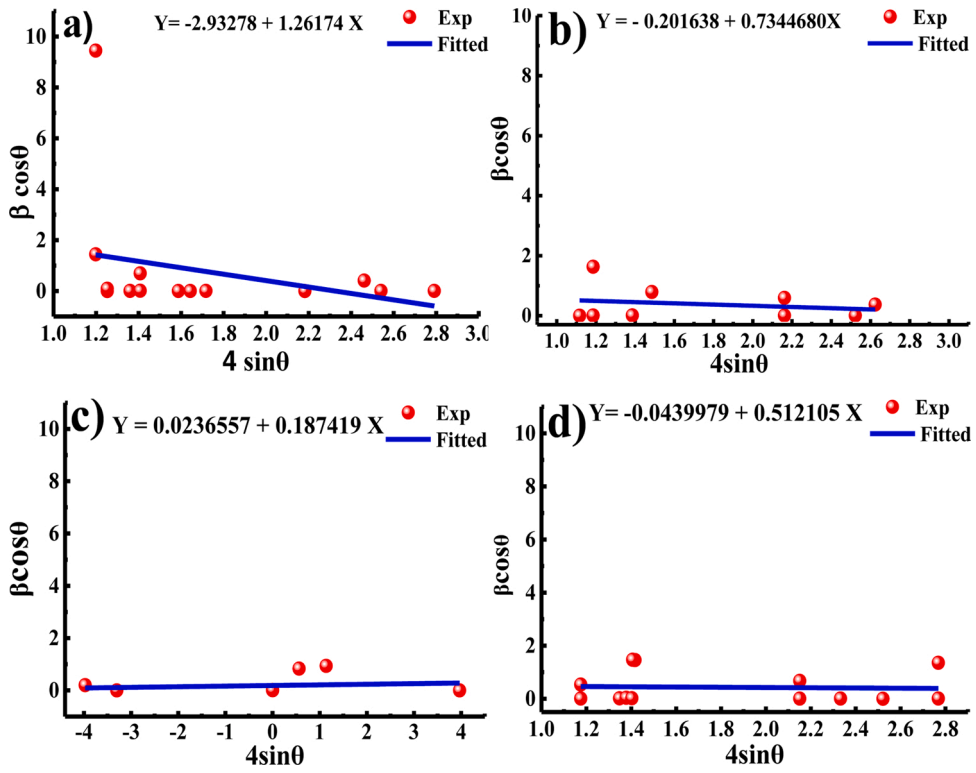

Fig. 7. Plots based on Williamson–Hall equation of the Ti-alloys, after different ball milling times. (a) 2 h, (b) 6 h, (c) 12 h and (d) 18 h. The experimental data are shown with symbols and fitted data are shown with solid line.

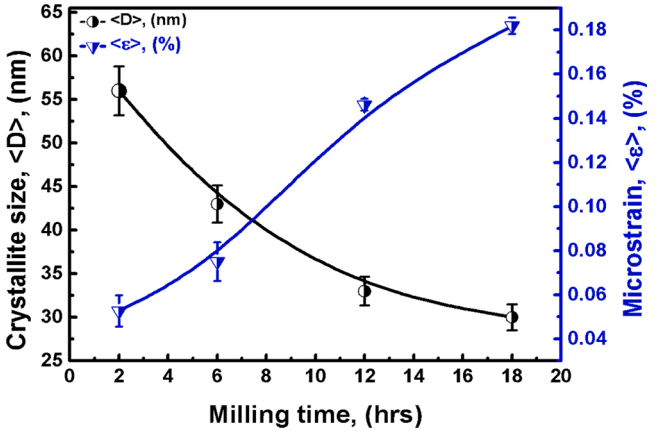

Fig. 8. Variation of crystallite size and lattice strain for Milled Ti-6Al-4Fe powders versus milling time.

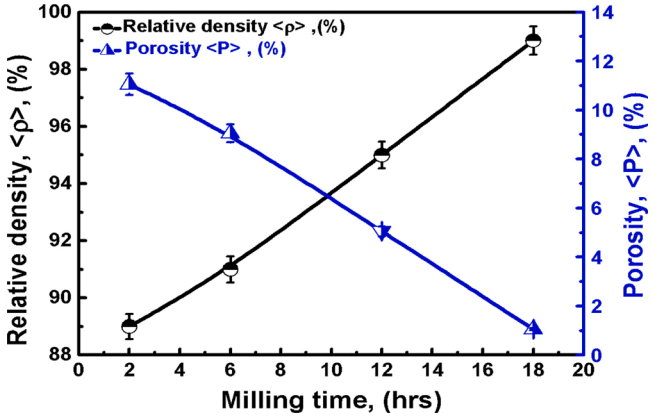

Fig. 9. Evolution of relative density (%) and porosity (%) of compacted and sintered samples as function of milling time. The theoretical density of the respective alloy is 4.532 $g \cdot cm^{-3}$.

attributed to the buildup of the strain energy [55,32]. Nouri et al. reported that enhanced microhardness due to grain refinement is most pronounced in the early stage of ball milling, whereas further increase is related to an increased grain size refinement, work hardening as well as the formation of supersaturated solid solutions [55].

Bones have a Young's modulus in the range of 17–28 GPa which is much lower than that of titanium alloys [56,43]. In titanium alloys, the Young's modulus increases with decreasing porosity [51]. The Young's modulus of the samples made of powders milled for 2 h and 6 h is 110 and 115 GPa, respectively which is similar to the values of the cp-Ti (105 GPa) and Ti-6Al-4V (110 GPa) [18]. The sintered samples made of powders milled for 12 h and 18 h have significantly higher Young's moduli (128 and 197 GPa, respectively). Young's moduli of representative titanium alloys are presented in Table 3 for comparison.

The sintered samples made of powders milled for 2 h reach the lowest value of Young's Modulus, making it more promising for their usage as a biomaterial [45,67,68,71]. Further modification of the alloy by addition of elements such as zirconium, tantalum and tin can contribute to the reduction of Young modulus [30].

3.2.3. *Surface roughness analysis*

The fatigue life of a work piece is significantly dependent on its surface roughness [35]. The surface roughness of sintered Ti-6Al-4Fe samples decreases with increasing milling time, which can be related to the increased hardness of the particles (Fig. 11). For the sintered specimens made of powders milled for 2 h, the roughness was Ra =7 nm which decreased to Ra =5 nm after 18 h of milling.

A porous bone scaffold, having a diversity in pore configuration and conformation, seems to be more tolerable in cellular and tissue

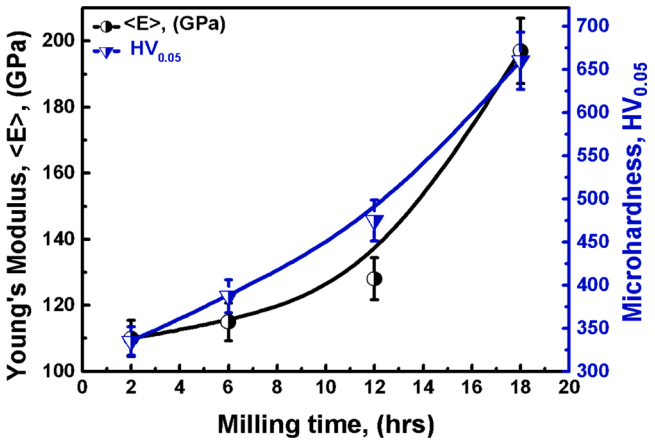

Fig. 10. Evolution of Vickers's hardness and Young's modulus for sintered Ti-6Al-4Fe samples versus milling time of the powders.

Table 3
Comparison of the Young's moduli of various compositions of titanium alloys.

Material	Manufacturing technique	Young's modulus (GPa)	References
cp-Ti	SLM	111.6 ± 2.7	[6]
Ti-6Al-4Fe	MA	110–197	In this work
TiTa	SLM	75.8 ± 4.0	[6]
Ti80Ni20	MA	130.7–164.5	[7]
Ti-6Al-4V	Standard	131.5 ± 16.4	[8]
	SLM	110	[6]
Ti-25Ta-25Nb	CCLM	55	[10]
Ti-15Ta-10.5Zr	SLM	42.9 ± 3.3	[11]
Ti-37Nb-6Sn	SLM	66	[13]
Ti–24Zr–4Nb–8Sn	SLM	53 ± 1	[22]
Ti4Al	MA	10–80	[24]
Ti-12Mo-6Zr-xFe	MA	93–105	[59]
Ti–37Nb–6Sn	SLM	66–78	[51]
Ti–50Ta	MA	100–130*	[62]

* Reduced Young's modulus.

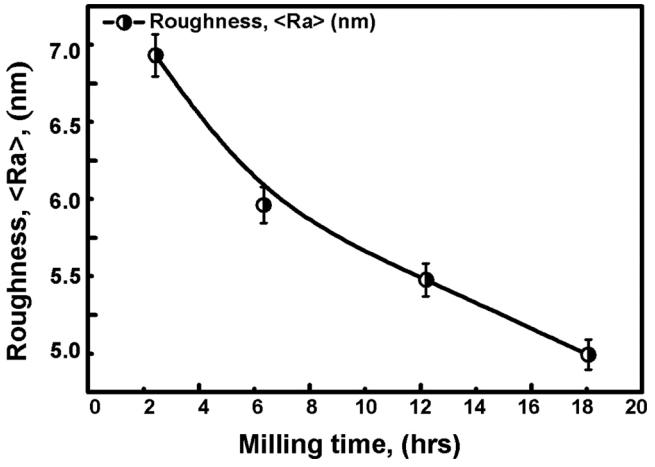

Fig. 11. Evolution of roughness analysis of sintered Ti-6Al-4Fe samples with milling time of the powders.

engineering than auto- or allografts [72]. The surface roughness has a significant effect on the morphology and proliferation of cells. Rougher topography is favorable for tissue growth and biocompatibility. Besides, a bone structure with micro-pores decreases stress-shielding effects, stimulating a favorable growth of tissue that allows fibroblasts to penetrate into the implant and help in forming new tissue within it.

On the other hand, flat implant surfaces prevent the adhesion of the opportune cells, which in turn, restrains the entire biocompatibility [56]. According to literature the growth of tissue on rough surfaces is different in comparison to cells growing on smooth surfaces. For example, primary rat osteoblasts had higher proliferation, ALP, and osteocalcin expression on a rougher surface than on a smoother one [9].

4. Conclusions

Morphological and mechanical properties of nanostructured Ti-6Al-4Fe alloys produces by powder metallurgy with varying ball milling times (2, 6, 8, 12 and 18 h) compacted and followed by sintering were studied. The following conclusions can be drawn from the obtained results:

- An increase in the lattice parameter values with increasing milling time was observed. Highest values were recorded for samples prepared from powders milled for 18 h.
- The crystallite size, calculated from XRD patterns using Scherrer's formula, gradually decreases with increasing milling time from 56 nm for 2 h milling time to 30 nm for 18 h milling time. This reduction resulted in a corresponding increase in microstrain within the Ti-6Al-4Fe alloys.
- The porosity of the Ti-6Al-4Fe alloys significantly decreases with an increase in milling time of the powders. Porosities between 1 % and 12 % were reached, which is comparable to that of a cortical bone. A reduction in porosity with increasing milling time of the powder resulted in an increase in density of the alloys.
- The microhardness of the alloys increased with increasing milling time of the powders and a maximum hardness of 660 $HV_{0.05}$ was obtained after 18 h of milling. In general, the developed Ti-6Al-4Fe alloys showed improved microhardness, compared to the commercial Ti-6Al-4 V alloy.
- The Young's modulus of the sintered Ti-6Al-4Fe alloys increased with increasing milling time of the powders, too.
- Surface roughness, an important parameter for biomaterials as it controls its functionality and its compatibility with cells and tissues, decreased with milling time of the powders for the developed Ti-6Al-4Fe alloys.

Authors statement

Hammadi Fouzia: Data curation, Writing- Original draft preparation. Investigation. **Mamoun Fellah:** Supervision, Writing- Reviewing and Editing, Visualization, Resources. **Naouel Hezil:** Data curation, Writing- Original draft preparation. **Linda Aissani**: Conceptualization, Methodology, Software. **Mimanne Goussem:** Reviewing and Editing. **Mechachti Said:** Data curation, Writing- Original draft preparation. **Mohammed Abdul Samad:** Writing- Reviewing and Editing. **Alex Montagne:** Resources. **Alain Iost:** Resources. **Sabine Weiß**: Supervision, Reviewing and Editing. **Aleksei Obrosov:** Reviewing and Editing.

Declaration of Competing Interest

The authors report no declarations of interest.

References

[1] M. Fellah, M. Labaïz, O. Assala, L. Dekhil, A. Iost, Tribological behavior of AISI 316L stainless steel for biomedical applications, Tribol.-Mater. Surf. Interf. 7 (2) (2013) 135–149.
[2] Y. Liu, F. Chen, G. Xu, Y. Cui, H. Chang, Correlation between microstructure and mechanical properties of heat-treated Ti–6Al–4V with Fe, Alloying Metals 10 (2020) 854.
[3] N. Hezil, M. Fellah, Synthesis structural and mechanical properties of nanobioceramic (α-Al_2O_3), J. Aust. Ceram. Soc. 55 (4) (2019) 1167–1175.

[4] L. Dekhil, N. Hanneche, M. Fellah, M. Bououdina, A.M. Mercier, Structural analysis and densification study of the mechanically alloyed $Cr_{50}Ni_{50}$ powders, Int. J. Adv. Manuf. Technol. 108 (2020) 2515–2524.

[5] M. Fellah, M. Labaïz, O. Assala, L. Dekhil, A. Iost, Friction and wear behavior of Ti-6Al-7Nb biomaterial alloy, J. Biomater. Nanobiotechnol. 4 (4) (2013) 374–384.

[6] P. Qi, B. Li, T. Wang, L. Zhou, Z. Nie, Microstructure and properties of a novel ternary Tie6ZrexFe alloy for biomedical applications, J. Alloys. Compd. 854 (2021), 157119.

[7] L. Dekhil, S. Louidi, M. Bououdina, M. Fellah, Microstructural, magnetic and nanoindentation studies of the ball-milled Ti80Ni20 alloy, J. Supercond. Nov. Magn. (2019), https://doi.org/10.1007/s10948-019-05145-1.

[8] B.D. Ratner, A.S. Hoffman, F.J. Schoen, J.E. Lemons, Biomaterials Science, Elsevier Academic Press, Oxford, 2004.

[9] L. Yan, Y. Yuan, L. Ouyang, H. Li, A. Mirzasadeghi, L. Li, Improved mechanical properties of the new Ti-15Ta-xZr alloys fabricated by selective laser melting for biomedical application, J. Alloys. Compd. 688 (2016) 156–162.

[10] M. Fellah, N. Hezil, M.Z. Touhami, M. Abdul Samad, A. Obrosov, D.O. Bokov, E. Marchenko, A. Montagne, A. Iost, A. Alhussein, Structural, tribological and antibacterial properties of (α + β) based Ti-Alloys for biomedical applications, J. Mater. Res. Technol. 9 (06) (2020) 1464–1471.

[11] M. Fellah, N. Hezil, D. Leila, M. Abdulsamad, R. Djellabi, S. Kosman, A. Montagne, A. Iost, A. Obrosov, S. Weiss, Effect of sintering temperature on structure and tribological properties of nanostructured Ti−15Mo alloy for biomedical applications, Trans. Nonferrous Metal. Soc. China 29 (11) (2019) 2310–2320.

[12] I. Simsek, D. Ozyurek, Investigation of the wear and corrosion behaviors of Ti-5Al-2.5Fe and Ti-6Al-4V alloys produced by mechanical alloying method in simulated body fluid environment, Innov. Corros. Mater. Sci. 1 (94) (2018) 357–363.

[13] W. Chen, C. Chen, X. Zi, X. Cheng, X. Zhang, Y.C. Lin, K. Zhou, Controlling the microstructure and mechanical properties of a metastable β titanium alloy by selective laser melting, Mater. Sci. Eng. A 726 (2018) 240–250.

[14] M. Fellah, N. Hezil, M.A. Hussein, M. Abdulsamad, M.Z. Touhami, A. Montagne, Alain IOST, A. Obrosov, S. Weiss, Preliminary investigation on the bio-tribocorrosion behaviour of porous nanostructured β-type titanium based biomedical alloy, Materials Letterss 257 (2019), 126755.

[15] L. Ding, R. Hu, Y. Gu, D. Zhou, F. Chen, L. Zho, Effect of Fe content on the As-Cast microstructures of Ti–6Al–4V–xFe alloy, Metals 10 (2020) 989.

[16] M. Fellah, L. Aissani, M. Abdul Samad, A. Iost, M.Z. Touhami, A. Montagne, C. Nouveau, Effect of replacing vanadium by niobium and iron on the tribological behavior of HIPed titanium alloys, Acta Metall. Sin. 30 (11) (2017) 1089–1099.

[17] L.S. Kim, Synthesis, Consolidation, and Mechanical Testing of Nanophase Metals, PhD. Thesis, UIUC, IL, 1997.

[18] P. Bhattacharya, P. Bellon, R.S. Averback, S.J. Hales, Nanocrystalline TiAl powders synthesized by high-energy ball milling effects of milling parameters on yield and contamination, J. Alloys. Compd. 368 (2004) 187–196.

[19] Z. Gao, H. Luo, Q. Li, Y. Wan, Preparation and characterization of Ti-10Mo alloy by mechanical alloying, Metallogr. Microstruct. Anal 1 (2012) 282–289.

[20] R.P. Siqueira, H.R.Z. Sandim, A.O.F. Hayama, V.A.R. Henriques, Microstructural evolution during sintering of the blended elemental Ti-5Al-2.5Fe alloy, J. Alloys. Compd. 476 (2009) 130–137.

[21] Y. Peng, Q. Zhu, T. Luo, J. Ca, Enhancement of the tensile strength by introducing alloy element Fe for Ti based alloy, Solid State Commun. 318 (2020), 113982.

[22] L.C. Zhang, D. Klemm, J. Eckert, Y.L. Hao, T.B. Sercombe, Manufacture by selective laser melting and mechanical behavior of a biomedical Ti-24Nb-4Zr-8Sn alloy, Scr. Mater. 65 (2011) 21–24.

[23] C. Suryanarayana, Mechanical alloying and milling, Prog. Mater. Sci. 46 (2001) 1–184.

[24] M. O. Bodunrin and L. H. Chown, Towards the development of experimental (α + β) Ti-Al-V-Fe alloys, Materials Today: Proceedings, https://doi.org/10.1016/j.matpr.2020.03.645.

[25] M. Fellah, N. Hezil, M.Z. Touhami, A. Obrosov, S. Weiß, E.B. Kashkarov, A. M. Lider, A. Montagne, A. Iost, Enhanced structural and tribological performance of nanostructured Ti–15Nb alloy for biomedical applications, Results Phys. 15 (2019), 102767.

[26] M. Fellah, N. Hezil, M. AbdulSamad, R. Djellabi, A. Montagne, A. Mejias, S. Kossman, A. Iost, A. Purnama, A. Obrosov, S. WeissS Sabine, Effect of molybdenum content on structural, mechanical, and tribological properties of hot isostatically pressed b-Type titanium alloys for orthopedic applications, J. Mater. Eng. Perform. 28 (10) (2019) 5988–5999.

[27] G. Liu, Z. Su, D. He, C. Lai, Wet ball-milling synthesis of high performance sulfur-based composite cathodes: the influences of solvents and ball-milling speed, Electrochim. Acta 149 (2014) 136–143.

[28] S. Wei, G. Zhu, C.C. Tasan, Slip-twin transfer across phase boundaries: an in-situ investigation of a Ti-Al-V-Fe (_C_) alloy, Acta Mater. 206 (2021), 116520.

[29] A. Wassilkowska, A. Czaplicka-Kotas, M. Zielina, A. Bielski, An Analysis of the elemental composition of micro-samples using EDS technique, Tech. Trans. Chem. (18) (2014) 133–148.

[30] S.A. Ibrahim, M.M. Seleman, H.M. Ahmed, A.E. Hannora, Phase stability of mechanically alloyed Ti-Fe-Al alloys, Mater. Sci. Eng. 973 (2020), 012025.

[31] M. Yang, Z. Guo, J. Xiong, F. Liua, K. Qi, Microstructural changes of (Ti, W) C solid solution induced by ball milling, J. Refract. Met. Hard Mater. 66 (2017) 83–87.

[32] T.F. Marinca, I. Chicinaş, O. Isnard, B.V. Neamţu, Nanocrystalline/nanosized manganese substituted nickel ferrites –Ni(1-x)MnxFe$_2$O$_4$ obtained by ceramic-mechanical milling route, Ceram. Int. 42 (2016) 4754–4763.

[33] U. Mehta, S.K. Yadav, I. Koirala, R.P. Koirala, D. Adhikari, Thermodynamic and surface properties of liquid Ti–Al–Fe alloy at different temperatures, Phys. Chem. Liquids (2020), https://doi.org/10.1080/00319104.2020.1793333.

[34] ISO 4287, Geometrical Product Specifications (GPS)-surface Texture: Profile Method-terms, Definitions and Surface Texture Parameters, International Organisation for Standardisation, Geneva, 1997.

[35] C. Suryanarayana, T. Klassen, E. Ivanov, Synthesis of nanocomposites and amorphous alloys by mechanical alloying, J. Mater. Sci. 46 (19) (2011) 6301–6315.

[36] A. Nouri, P.D. Hodgson, C. Wen, Effect of ball-milling time on the structural characteristics of biomedical porous Ti-Sn-Nb alloy, Mater. Sci. Eng. 31 (2011) 921–928.

[37] X. Li, C. Guan, P. Zhao, Influences of milling and grinding on machined surface roughness and fatigue behavior of A GH4169 superalloy workpiece, Chinese J. Aeronaut. 31 (6) (2017) 1399–1405.

[38] B. Tomiczek, L.A. Dobrzasanki, M. Adamiak, K. Labisz, Effect of milling conditions on microstructure and properties of AA6061/Halloysite composites, Procedia Manuf. 2 (2015) 402–407.

[39] S.G. Sarwat, Contamination in wet-ball milling, Powder Metall. 60 (2017) 267–272.

[40] M.G. Raucci, V. D'Antò, V. Guarino, E. Sardella, S. Zeppetelli, P. Favia, L. Ambrosio, Biomineralized porous composite scaffolds prepared by chemical synthesis for bone tissue regeneration, Acta Biomater. 6 (10) (2010) 4090–4099.

[41] L. Li, F.T. Zi, Y.F. Zheng, The characterization of fluorocarbon films on NiTi alloy by magnetron sputtering, Appl. Surf. Sci. 255 (2008) 432–434.

[42] A. Adamczy, K. Długoń, The FTIR studies of gels and thin films of Al_2O_3-TiO_2 and Al_2O_3-TiO_2-SiO_2 systems, Spectroscopy 89 (2012) 11–17.

[43] I.V. Pylypchuk, A.L. Petranovskaya, P.P. Gorbyk, A.M. Korduban, P.E. Markovsky, O.M. Ivasishin, Biomimetic hydroxyapatite growth on functionalized surfaces of Ti-6Al-4V and Ti-Zr-Nb alloys, Nanoscale Res. Lett. 10 (2015) 338.

[44] Z. Song, E. Chouparova, K.W. Jones, H. Feng, N.S. Marinkovic, FTIR Investigation of Sediments From NY/NJ Harbor, San Diego Bay, and the Venetian Lagoon, NSLC Activity Report, Science Highlights, 2001, pp. 112–116.

[45] J. Sabatatyté, I. Oja, F. Lenzman, O. Volobujeva, A. Krunks, Characterization of nanoporous /TiO_2 films prepared by sol-gel method, Comptes Rendus Chim. 9 (5-6) (2006) 708–712.

[46] N. Ajmal, K. Saraswat, A. Bakht, Y. Riadi, M. Ahsan, M. Noushad, Cost-effective and eco-friendly synthesis of titanium dioxide (TiO_2) nanoparticles using fruit's peel agro-waste extracts : characterization,in vitro antibacterial, antioxidant activities, Green Chem. Lett. Rev. 12 (3) (2019) 244–254.

[47] M. Takafuji, M. Kajiwara, N. Hano, Y. Kuwahara, H. Ihara, Preparation of high refractive index composite films based on titanium oxide nanoparticles hybridized hydrophilic polymers, Nanomaterials 9 (4) (2019) 514.

[48] O.S. Ogbonna, S.A. Akinlabi, N. Madushele, P.M. Mashinini, A.S. Afolalu, Effect of milling time on the morphological evolution of titanium alloy powder, Editorial 1378 (4) (2019), 042066.

[49] M. Fellah, M. Abdul Samed, M. Labaïz, O. Assala, L. Dekhil, A. Iost, Sliding friction and wear performance of the nano-bioceramic α-Al_2O_3 prepared by high energy milling, Tribol. Int. 91 (2015) 151–159.

[50] M.K. Han, M.J. Hwang, D.H. Won, Y.S. Kim, H.J. Song, Y.J. Park, Massive Transformation in titanium-silver alloys and its effect on their mechanical properties and corrosion behavior, Materials Basel (Basel) 7 (9) (2014) 6194–6206.

[51] E. Sakher, N. Loudjani, M. Benchiheub, M. Bououdina, Influence of milling time on structural and microstructural parameters of Ni50Ti50 prepared by mechanical alloying using rietveld analysis, Journal of Nanomaterials (2018) 1–11.

[52] M.T. Jia, B. Gabbitas, L. Bolzoni, Evaluation of reactive induction sintering as a manufacturing route for blended elemental Ti-5Al-2.5Fe alloy, J. Mater. Process. Technol. 255 (2018) 611–620.

[53] W. Chen, C. Chen, X. Zi, X. Cheng, X. Zhang, Y.C. Lin, K. Zhou, Controlling the microstructure and mechanical properties of a metastable β titanium alloy by selective laser melting, Mater. Sci. Eng. A 726 (2018) 240–250.

[54] M. Yang, Z. Guo, J. Xiong, F. Liu, K. Qi, Microstructural changes of (Ti, W) C solid solution induced by ball milling, J. Refract. Met. Hard Mater. 66 (2017) 83–87.

[55] C. Wang, B.L. Cheng, S.Y. Wang, H.B. Lu, Y.L. Zhou, Z.H. Chen, G.Z. Yang, Effects of oxygen pressure on lattice parameter, orientation, surface morphology and deposition rate of (Ba0.02Sr0.98) TiO_3 thin films grown on MgO substrate by pulsed laser deposition, Thin Solid Films 485 (2005) 82–89.

[56] G. Liang, R. Schulz, Synthesis of Mg-Ti alloy by mechanical alloying, J. Mater. Sci. 38 (2003) 1179–1184.

[57] D. Zaworonkow, M. Chekan, K. Kusnierz, A. Lekstan, A. Grajoszek, Z. Lekston, D. Lange, T. Chekalkin, J. Kang, V. Gunther, Evaluation of TiNi-based wire mesh implant for abdominal wall defect management, Biomed. Phys. Eng. Express 4 (2) (2018), 027010.

[58] Y. Long, H. Zhang, T. Wang, X. Huang, Y. Li, J. Wu, H. Chen, High-strength Ti-6Al-4V with ultrafine-grained structure fabricated by high-energy ball milling and spark plasma sintering, Mater. Sci. Eng. A 585 (2013) 408–414.

[59] G. Rajender, P.K. Giri, Strain induced phase formation, microstructural evolution and bandgap narrowing in strained TiO_2 nanocrystals grown by ball milling, J. Alloys. Compd. 676 (2016) 591–600.

[60] C. Salvo, C. Aguilar, R. Cardoso-Gil, A. Medina, L. Bejar, R.V. Mangalaraja, Study on the microstructural evolution of Ti-Nb based alloy obtained by high-energy ball milling, J. Alloys. Compd. 720 (2017) 254–263.

[61] B. Avar, S. Ozcan, Structural evolutions in Ti and TiO_2 powders by ball milling and subsequent heat-treatments, Ceram. Int. 40 (7) (2014) 11123–11130.

[62] S.S. Razavi Tousi, R. Yazdani Rad, E. Salahi, I. Mobasherpour, M. Razavi, Production of Al-20 wt % Al_2O_3 composite powder using high energy milling, Powder Technol. 192 (2009) 346–351.

[63] H. Yu, Y. Sun, L. Hu, H. Zhou, Z. Wan, Microstructural evolution of AZ61-10 at. % Ti composite powders during mechanical milling, Mater. Sci. Eng. (104) (2016) 883–891.
[64] G. Dercz, I. Matułaa, M. Zubkoa, A. Kazek-Kęsikb, J. Maszybrockaa, W. Simka, J. Derczc, P. Świeca, I. Jendrzejewskad, Synthesis of porous Ti-50Ta alloy by powder metallurgy, Mater. Charact. 142 (2018) 124–136.
[65] D. Junhui, M. Wen, S. Zhiming, Progress in materials and processes: selected, Peer Reviewed Papers from the 2nd International Conference on Materials and Products Manufacturing Technology (2013) 602–604.
[66] R.B. Martin, Porosity and specific surface of bone, Crit. Rev. Biomed. Eng. 10 (1984) 179–222.
[67] G. Dercz, I. Matuła, J. Maszybrocka, M. Zubko, J. Barczyk, L. Pająk, S. Stach, Effect of milling time and presence of Sn on the microstructure and porosity of sintered Ti-10Ta-8Mo and Ti-10Ta-8Mo-3Sn alloys, J. Alloys. Compd. 791 (2019) 232–247.
[68] O. Kokorev, V. Hodorenko, T. Chekalkin, V. Gunther, S.B. Kang, M.J. Chang, J. H. Kang, Evaluation of allogenic hepato-tissue engineered in porous TiNi-based scaffolds for liver regeneration in a CCl_4-induced cirrhosis rat model, Biomed. Phys. Eng. Express 5 (2) (2019).
[69] I. Simsek, D. Ozyurek, Investigation of the wear and corrosion behaviors of Ti-5Al-2.5Fe and Ti6Al4V alloys produced by mechanical alloying method in simulated body fluid environment, Mater. Sci. Eng. C 94 (2018) 357–363.
[70] R. Yamanoglu, E. Efendi, I. Daoud, Sintering properties of mechanically alloyed Ti-5Al-2.5Fe, world academy of science, engineering and technology, Int. J. Mater. Metall. Eng. 11 (5) (2017) 309–313.
[71] N. Sezer, Review of magnesium-based biomaterials and their applications, J. Magnes. Alloy. 6 (1) (2018) 23–43.
[72] Y. Yasenchuk, E. Marchenko, V. Gunther, A. Radkevich, O. Kokorev, S. Gunther, G. Baigonakova, V. Hodorenko, T. Chekalkin, J.-H. Kang, S. Weiss, A. Obrosov, Biocompatibility and clinical application of porous TiNi alloys made by self-propagating high-temperature synthesis (SHS), Materials 12 (15) (2019) 2405.